Reprinted from Applied Optics, Vol. 25, Page 2835, August 15, 1986

22

Computer controlled polishing and testing of a glancing incidence telescope

Roger J. Thomas, Geraldine A. Wright, and Charles M. Fleetwood

The elements of a Wolter type II telescope have been fabricated using a small area tool in a computer controlled facility. The absolute radius of the mirrors can be established to 0.812 μm, and relative heights on the surfaces can be determined to 0.016 μm. The primary has a 0.041-μm rms surface error, and the secondary has a 0.054-μm surface error.

I. Introduction

The purpose of the current study of computer controlled polishing and testing of glancing incidence optics is to demonstrate the feasibility of fabricating the telescope for the proposed solar extreme ultraviolet telescope and spectrograph (SEUTS).[1,2] This instrument is designed to obtain images and spectra of active regions on the sun in the 22–44-nm spectral region, and it requires imaging capabilities of 2 sec of arc over a 4-min of arc field of view.

Glancing incidence telescopes are required for operation in this wavelength range because the reflectivity of normal incidence coatings is low, particularly for wavelengths shorter than 50 nm.[3,4] Some work has been done to increase the reflectance of normal incidence mirrors with layered synthetic microstructures (LSMs),[5–9] in which the refractive index varies periodically with depth. Ir-Si LSMs show enhanced reflectivity at extreme-UV wavelengths but have narrow bandwidths. In addition, it has not been demonstrated that these coatings are stable in the space environment. For these reasons, a Wolter type II[10] glancing incidence telescope was selected for the SEUTS instrument.

To produce a glancing incidence telescope with 2-sec of arc imaging, new testing procedures need to be developed to measure surface figure errors. Traditional interferograms, in which figure errors are projected into a plane perpendicular to the optical axis, record the surface figure information in a plane which makes large angles with the optical surface. This compresses the data axially, as shown in Fig. 1, making it difficult to interpret. Even if it can be interpreted, the large cosine errors involved in mapping the deviations from the interferogram onto the mirror make the axial positions of the surface deviations very sensitive to small errors in measuring fringe position on the interferogram. Cylindrical test plates, which may be used to test Wolter type I mirrors, are unsuitable for Wolter type II optics because they depart significantly from cones, producing high fringe densities that make interferograms difficult to interpret.

In addition to new test procedures, new polishing procedures must be found. In our experience, hand figuring produces glancing incidence telescopes with 5-sec of arc imaging at best. Thus an automated procedure is being developed in which the amount of polishing at each location is reproducibly controlled by the error at that location. Efforts to automate the polishing process are being conducted at various places.[11,12] The following discussion describes the effort at Goddard Space Flight Center to automate the fabrication of glancing incidence mirrors. A schematic of the telescope being fabricated is shown in Fig. 2, and the individual elements are shown in Fig. 3.

II. Generating and Grinding

The first step in fabricating the elements is to generate and grind the surfaces. The general shape is ground into the blank using an edge grinder, as shown in Fig. 4. The ends of the cylindrical blank are ground flat and parallel, after which they serve as references to align the blank with the axis of the edge grinder. Cones, whose angles equal the average grazing angle of the mirrors, are ground into the cylindrical blanks. An internal cone is generated for the parabola and an external cone for the hyperbola. In addition to the cones, any external shaping of the parabola is done at this point. The blanks are oversized axially so that the turned down edge (a residual from final grinding) may be cut off before assembly. Extra material is left so that subsequent grinding and polishing do not cause the surface to fall below the design curve. After generating the rough shapes, the mirrors are acid etched to relieve stress introduced during grinding.[13]

Once the cones have been generated, the parabolic and hyperbolic shapes are ground into the blanks using loose abrasive and plunge laps made of brass, two of which are seen in Fig. 5. These laps were produced on numerically controlled precision lathes and have a profile that matches the desired optical element. Once

The authors are with NASA Goddard Space Flight Center, Greenbelt, Maryland 20771.

Received 17 April 1986.

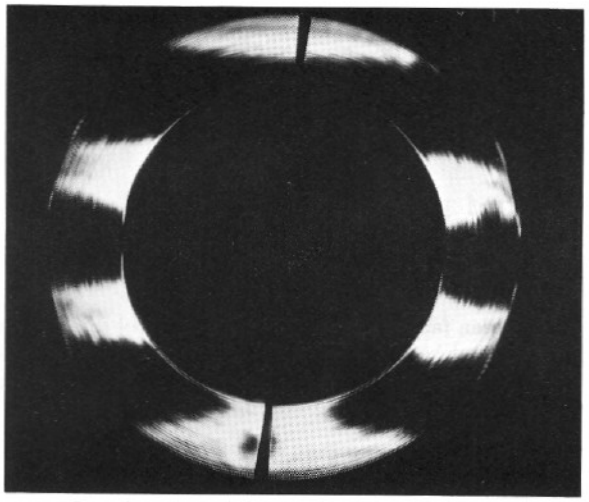

Figure 1. Interferogram of glancing incidence mirror taken in same manner as for a normal incidence mirror. Data are compressed axially making it difficult to interpret. The large cosine factors also make the axial positions sensitive to small errors in measuring fringe location.

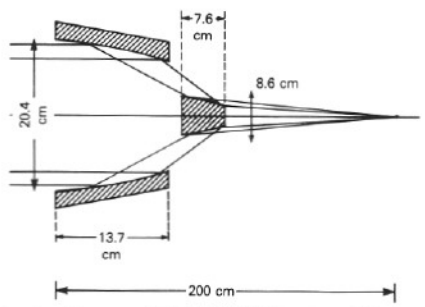

Figure 2. Optical layout of SEUTS Wolter type II telescope. Focal length is 450 cm.

machined, the laps are measured and hand lapped to bring their profiles closer to the desired curve. Two laps are required for each mirror. The first is used to rough grind the mirror, and the second is used for fine grinding.

During grinding the optical surface is ground against the matching lap to impart the proper shape to the glass, as shown in Fig. 6. The interior of the parabolic blank is ground against the exterior of its lap, and the exterior of the hyperbolic blank is ground against the interior of its lap. The grinding proceeds through a series of successively finer grit sizes, each grinding stage lasting long enough to remove completely the damaged layer left by the previous grade, whose depth is three times the size of the particles in the previous grade of grit.[14] This ensures that the depth of the damaged layer is always known and after final grinding is shallow enough to be removed by polishing. The mirror is ground to the desired curve, a point which is determined by measuring the mirror diameter at a given axial position.

The advantage of plunge lapping is that by rotating both the lap and element, errors not symmetrical about the optical axis are averaged out, so that only

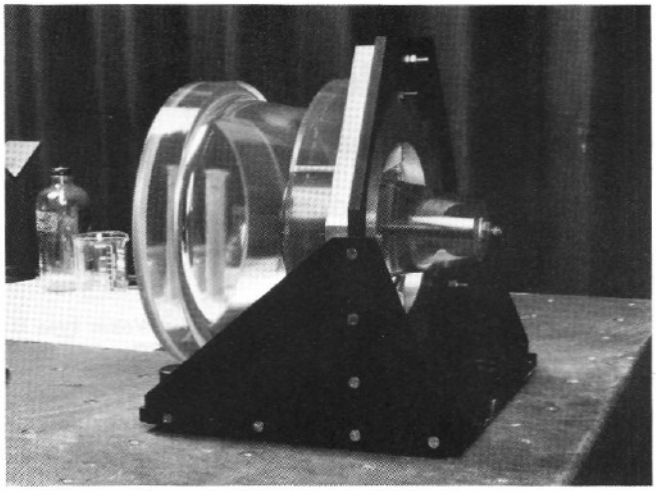

Figure 3. Individual elements.

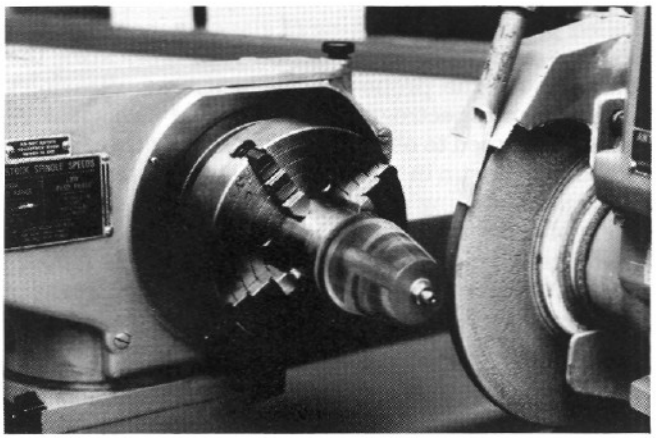

Figure 4. Edge grinding setup.

Figure 5. Plunge laps used to grind the conic shapes into mirrors.

errors of axial dependence need to be addressed during polishing. Figure 7 shows the out of roundness error on the mirrors after the final grinding stage. After final grinding, the ends are reground and polished flat and perpendicular to the optical axis. Also, fiducial marks, which will be described, are inscribed on the mirror blank.

Figure 6. Plunge lapping.

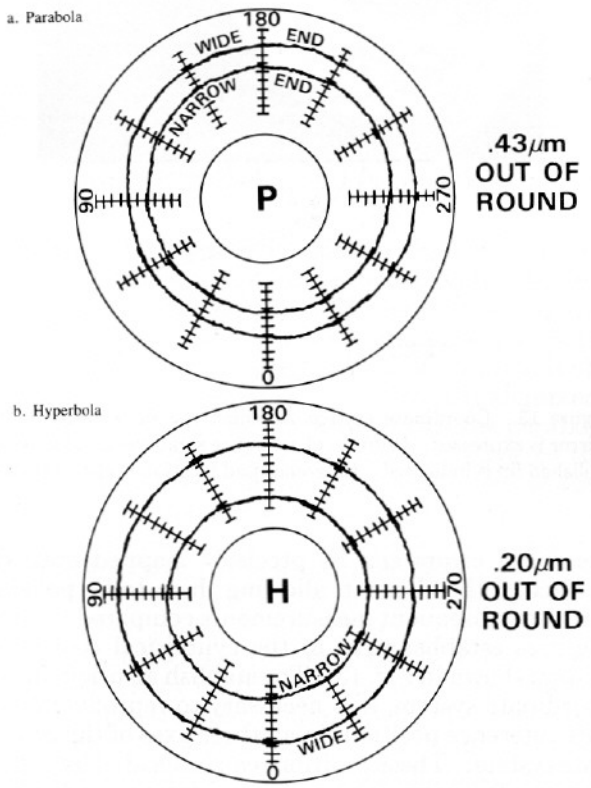

Figure 7. Azimuthal error of elements of SEUTS telescope after the final grinding stage.

III. Metrology

Once the blanks have been ground, a precision measuring machine is used to obtain the axial profile of the mirror. The setup is shown in Fig. 8, and the parts of the setup are identified in Fig. 9. The Moore 3 measuring machine has lead screws driven by a stepper motor controller. An HP-5501 interferometer with a resolution of 0.016 μm monitors the movement of the machine slide table. An inductance-type electronic ball probe with a 0.8-mm diam ball is installed on the vertical spindle of the machine to measure the axial profile. A set of Cartesian coordinates is superposed on the machine axes as shown in Fig. 9.

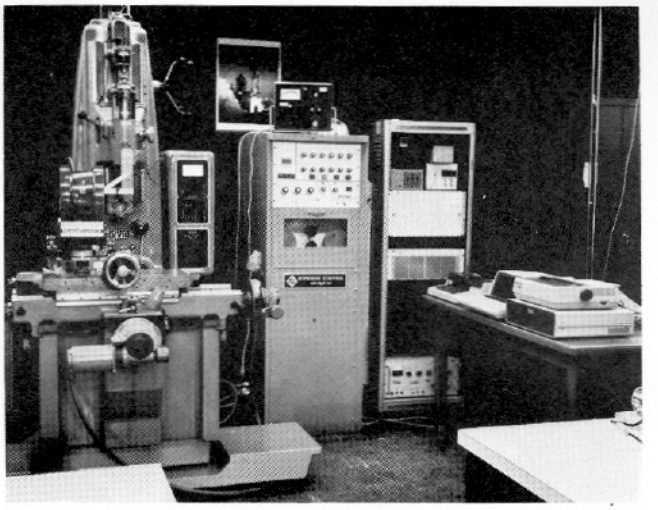

Figure 8. Setup used to measure glancing incidence mirrors.

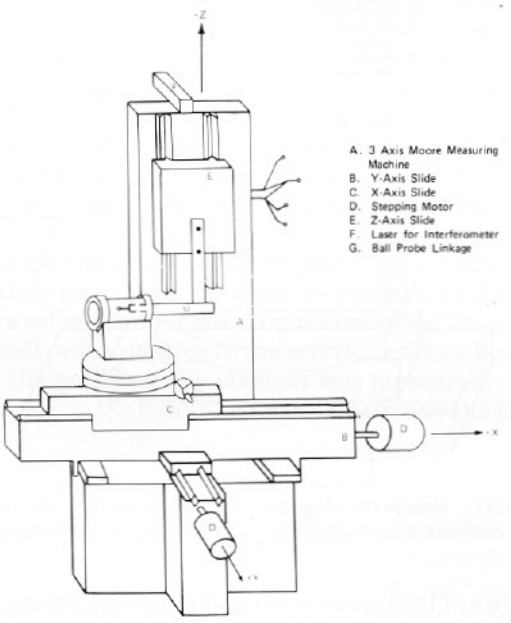

Figure 9. Schematic diagram of the measurement setup. Machine axes are labeled.

Figure 10 shows a close-up of the parabola setup on the slide table for a measurement with the various parts of the setup identified in Fig. 11. A rotary table is bolted to the Moore machine X slide, and a tilt plate is attached to the rotary table with magnets. A v-block is set on the tilt plate, and the parabola is mounted in the v-block with its optical axis parallel to the x axis. The probe, which is attached at the end of an arm so it can reach the optical surface, contacts the surface and is oriented to measure displacements parallel to the y axis. The stepping motors advance the lead screws to step the mirror along the theoretical curve, which is stored on a flexible disk. The probe measures deviations from the theoretical curve, and the interferometer monitors the actual position of the slide table, which may differ from the nominal position

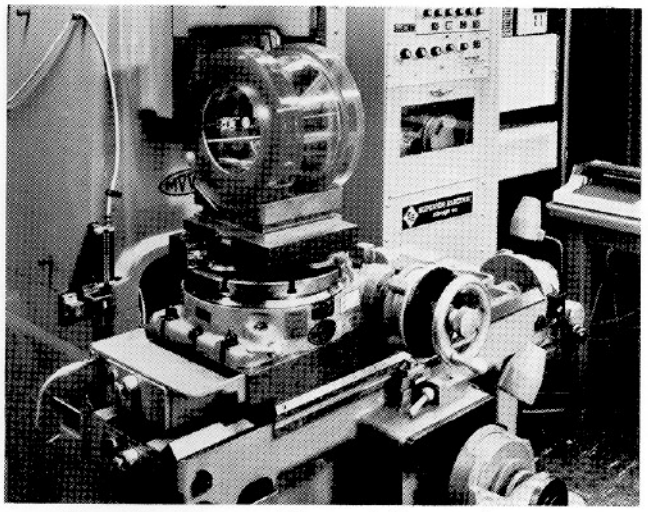

Figure 10. Close-up of the parabola on testing mount.

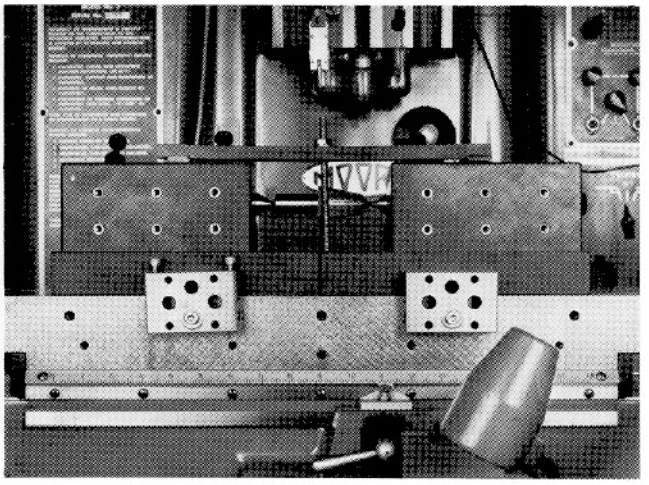

Figure 12. Measurement setup for the hyperbola.

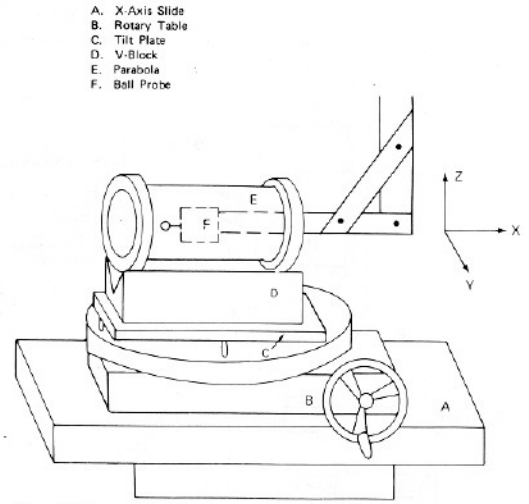

Figure 11. Schematic diagram of parabola on test mount. Machine axes are indicated: (a) parabola; (b) hyperbola.

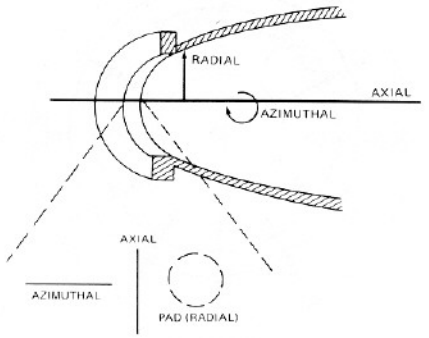

Figure 13. Coordinate system in which the figure error of the mirror is expressed. Position of reference scratches on ground and polished lip is indicated. Reference pad location is also indicated.

because of lead screw error and temperature expansion of the lead screw. The entire system is controlled by an HP-87 computer. Probe readings are fed into an amplifier which has a noise level of 0.00254 μm and then into an analog–digital converter, which sends the digitized voltages to the computer. The interferometer and surface data are then stored on a flexible disk.

The measurement setup for the hyperbola, which is shown in Fig. 12, is similar to that for the parabola. The main difference in the setup is the mount for the hyperbola itself. The hyperbola is mounted onto a precision ground shaft by means of a threaded rod through the center of the hyperbola. It can be suspended between points with its optical axis parallel to the machine x axis. The points are on the ends of two rods which are secured to granite blocks, which are in turn bolted to the slide table. The probe contacts the optical surface and measures deviations from the theoretical curve.

To measure the mirrors, a technique must be developed to reproducibly establish fiducials so that the measured errors can be precisely mapped onto the surface of the element, allowing them to be polished out and subsequent measurements compared.[15] This requires establishment of the cylindrical coordinate system shown in Fig. 13. To establish an origin in this coordinate system, it is necessary to reproducibly locate reference positions in all three axes of the coordinate system. These positions can be located by the use of two reference scratches and a reference pad, whose locations on the cylindrical blank are shown in Fig. 13. The scratches allow the axial and azimuthal reference origins to be established. The reference pad, a spot on the ground and polished lip with a predetermined position relative to the scratches, is a known distance from the optical axis and so allows a radial reference position to be established.

The first step in establishing the fiducials on the mirror is to align the optical axis to the x axis. The mirror is placed in its mount with the optical axis approximately aligned to the x axis. The probe is placed in contact with the optical surface oriented so that it measures deviations parallel to the y axis. It is moved vertically until an extremum in the probe deviation is obtained, at which point the radial plane has been found. The x axis is moved to bring the probe to

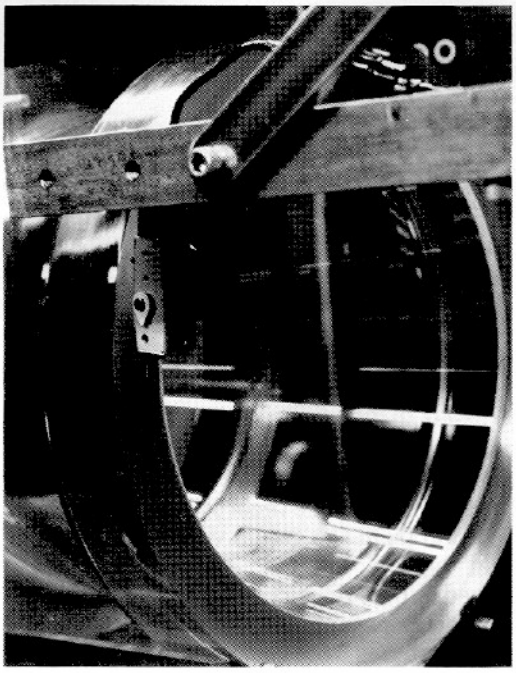

Figure 14. Measuring tilt of the optical axis.

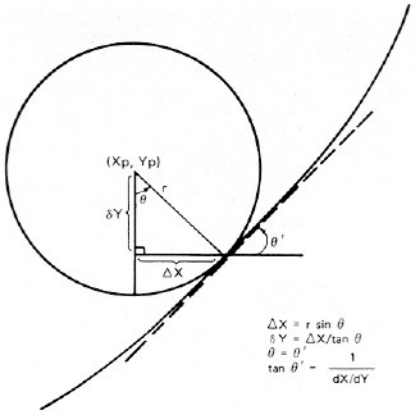

Figure 15. Geometry of the calculation of glass coordinates from the position of ball center.

the vicinity of the scratches, and the element is rotated about its optical axis until the probe is centered in the azimuthal reference scratch. This locates the origin of the azimuthal coordinate in the reference coordinate system. After the proper azimuthal orientation is obtained, fine adjustments can be made to the alignment of the optical axis. The operator adjusts the parabola by probing its endface, whose angle relative to the optical axis has been measured previously, and adjusting the angle of the endface relative to the x and y axes using the tilt plate and rotary table, as shown in Fig. 14. The optical axis can be aligned to within 0.1 sec of arc.

After the optical axis is aligned, the fiducials may be located. The probe is moved back into the radial plane, and the element is moved axially using the machine lead screws until the probe is centered in the axial reference scratch. The x axis leg of the interferometer is zeroed at this point. This establishes the axial reference in the reference coordinate system. It can be reproducibly located to within 2.54 μm. Finally, the element is moved axially a known distance to the position of the reference pad and then radially to zero the probe. The y-axis leg of the interferometer is zeroed, and the radial origin has now been located. Since the radial position of the reference pad is known from previous measurement, all measurements can be referred to the optical axis. The radial origin can be reproducibly located to within 0.812 μm. This procedure allows one to measure the figure error in a coordinate system with its origin on the optical axis at the azimuthal position of the horizontal reference scratch and at the axial position of the vertical reference scratch.

Once the fiducials have been found, which is done by the operator with prompts from the computer console, the motors step the element past the probe. At each position the element is allowed to sit for ~4 s to allow it to stabilize. Readings are taken from the X and Y legs of the interferometer and from the probe. The X reading gives the X position of the center of the ball probe directly. Subtracting the probe reading from the Y reading gives the Y position of the ball center. After the readings are taken and the X and Y coordinates of the ball center have been calculated, the stepper motor controller drives the lead screws to the next location on the mirror. When the element has been completely measured, the data are stored on a flexible disk as a set of X and Y coordinates denoting the center of the ball probe relative to the reference scratches and pad as the profile of the element was measured. The uncertainty in the height of errors relative to the reference pad is 0.016 μm.

IV. Data Reduction

The raw data stored on disks may be reduced to determine the actual glass profile from the coordinates of the center of the ball probe. The probe will contact the glass at the point where their slopes are equal, so that once the slope at the contact point has been calculated, the corrections needed to obtain the glass surface coordinates can be found. The geometry is shown in Fig. 15.

The slope, or dY/dX, is calculated from the coordinates of the ball center. The Y coordinate of the ball center is found using the formula

$$Y_p(I) = Y_r(I) + Y_r, \tag{1}$$

where $Y_p(I)$ = radial coordinate of the ball center for the Ith measurement point,
$Y_r(I)$ = radial distance of the ball center from the reference pad for the Ith point, and
Y_r = radial distance of the reference pad from the optical axis.

The slope dX/dY may then be calculated using the formula

$$dX/dY = D = [X_p(I+1) - X_p(I)]/[Y_p(I+1) - Y_p(I)], \tag{2}$$

where $X_p(I+1)$ = axial coordinate of the ball center at

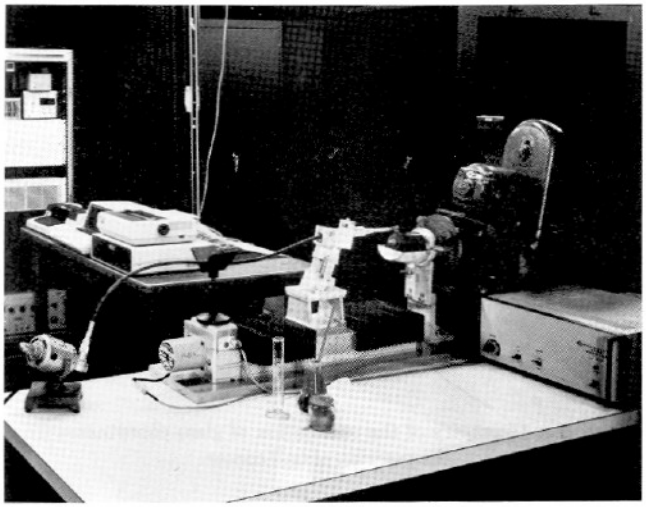

(a)

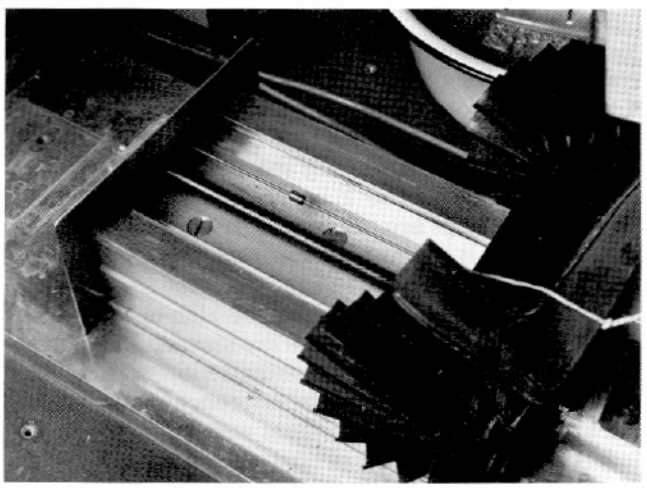

(b)

Figure 16. Setup used to polish glancing incidence mirrors: (a) entire setup; (b) close-up with bellows pulled back to expose lead screw.

the $(I + 1)$th point and $X_p(I)$ = axial coordinate of the ball center at the Ith point.

Once the slope is found, the value ΔX, which is needed to obtain the axial coordinate of the point at which the ball contacts the glass surface, can be found from

$$\Delta X = r/(1 + D^2)^{1/2}, \tag{3}$$

where r is the radius of the ball on probe.

The actual glass coordinates may then be found by using

$$\left.\begin{aligned} X_g(I) &= (X_p(I + 1) + X_p(I)/2 + S\Delta X, \\ Y_g(I) &= [Y_p(I + 1) + Y_p(I)]/2 - S\Delta XD, \end{aligned}\right\} \tag{4}$$

where $X_g(I)$ = axial coordinate of the ball contact with the optical surface at the Ith point,

$Y_g(I)$ = radial coordinate of the ball contact with the optical surface at the Ith point, and

$$S = \begin{cases} -1, \text{ for parabola} \\ +1, \text{ for hyperbola.} \end{cases}$$

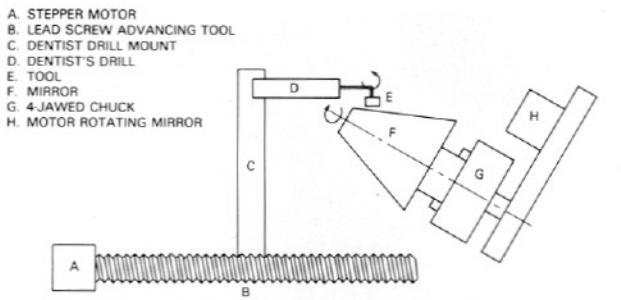

Figure 17. Schematic diagram of polishing setup with parts identified. The tool rotates about a vertical axis, and the mirror rotates about its optical axis.

This now gives the desired surface profile data. The deviation of the surface from the design curve may be found by subtracting the theoretical value of Y_g at each axial position from the actual value of Y_g at that position.

If desired, a best fit curve may be found by optimizing the conic constants and the axial distance of the reference scratches from the conic foci to minimize the rms deviation of the data from the best fit curve. In other words, the quantity to be minimized is

$$E = \left(\sum_{I=0}^{N} \{[Y_g(I) - Y_t(I)]^2/N\}\right)^{(1/2)}, \tag{5}$$

where $Y_g(I)$ = value of Y_g at the Ith value of X_g;

$Y_t(I)$ = theoretical value of Y_g at the Ith value of X_g using best fit parameters; and

N = total number of measurements.

To minimize the rms surface error, we use a method that reduces to zero the values of the partial derivatives of the error function with respect to the parameters to be optimized.[16] Once the best fit values for the curves have been found, the rms deviation may be calculated by subtracting the theoretical values from the actual ones.

V. Polishing

Once the mirror has been measured, it can be polished. The element is polished and figured by a small diameter (6.4-mm) tool which dwells at an axial position long enough to remove the error at that position and then moves to another axial position. This setup is shown in Fig. 16, and a schematic diagram is shown in Fig. 17. The element is mounted on a 4-jaw chuck on the shaft of a motor; the hyperbola is mounted using the metal shaft to which it is attached, while the parabola is placed into a cylinder large enough to completely contain it and is then mounted in the chuck. This allows the mirrors to be chucked onto the motor shaft without putting a load directly on the mirror. The mirror is rotated about its axis at 34 rpm (hyperbola) or 38 rpm (parabola). The tool, which can be seen in the close-up in Fig. 18, is a piece of felt impregnated with pitch and mounted in a dentist's drill which rotates it at 1620 rpm and which is held against the mirror by a spring. The drill is mounted on a platform which is driven by the horizontal lead screw.

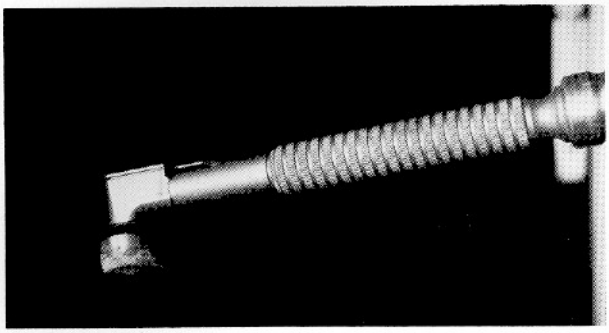

Figure 18. Close-up of polishing tool.

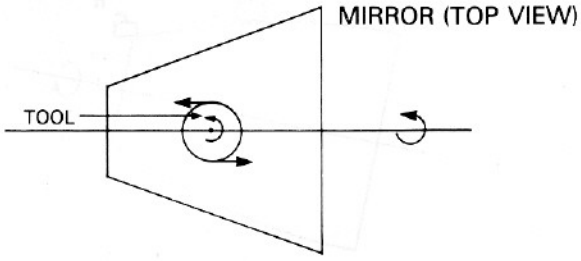

a. Relative motion between glass and sides of tool will try to polish grooves parallel to the optical axis. But rotation of the mirror prevents the tool from dwelling at an azimuthal position long enough to form grooves.

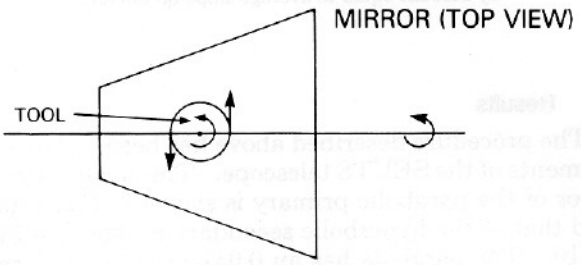

b. Relative motion between glass and front and back of tool will try to polish grooves perpendicular to the axis. Axial motion of tool is slow enough for grooves to form.

Figure 19. Tool polishing flat against the glass will form grooves on the surface.

If allowed to polish flat against the glass, the tool will polish a set of grooves concentric about its spin axis. During a run, the tool will try to polish grooves into the mirror, some of which are parallel to the optical axis and some of which are perpendicular to the axis. Because of the rotation of the mirror, the tool is not allowed to linger over an azimuthal position long enough for the grooves parallel to the axis to form, as can be seen in Fig. 19(a). But the axial motion of the tool over the mirror is much slower, so the grooves perpendicular to the axis do have long enough to form, as shown in Fig. 19(b). To prevent this, the dentist's drill holding the tool is rotated ~5° about a horizontal axis, as shown in Fig. 20(a). Only one side of the tool contacts the mirror, so that the relative motion between the tool and mirror at the point of contact is parallel to the optical axis, as seen in Fig. 20(b). This is the motion that produces the grooves parallel to the axis, which do not have a chance to form anyway. The

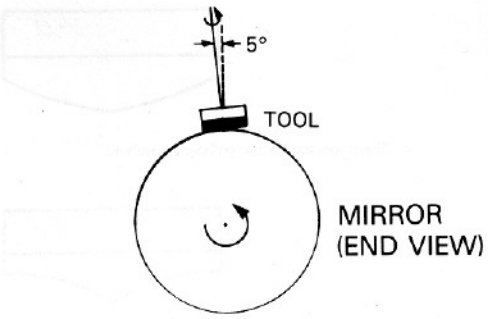

a. Rotating the dentist's drill about the horizontal causes the tool to contact the mirror only along one side.

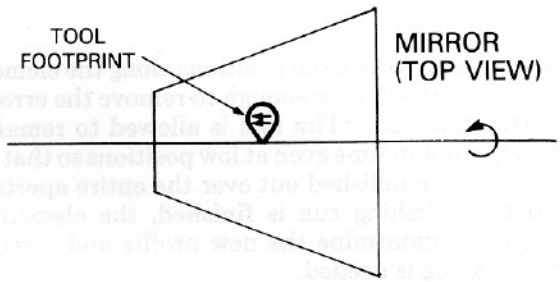

b. Footprint of tool on glass is tear shaped. Relative motion between tool and glass within footprint tries to form grooves parallel to the optical axis.

Figure 20. Tilting the drill allows the tool to contact only along one side.

tool does not contact the mirror at those points at which its relative motion with the mirror would polish grooves perpendicular to the axis, thus these grooves are prevented. The net result is to prevent formation of the grooves on the mirror.

Rotating the tool against the surface at an angle causes the tool to assume a conical shape, as shown in Fig. 21. Because of the conical shape and because only one side of the tool contacts the mirror, polishing takes place in a narrow axial zone, so the tool contact can be adequately approximated as a point.

Bowl feed polishing techniques[17] are used to maintain a constant uniform bath of cerium oxide solution on the element during polishing. For the parabola, the bath is created by damming the ends with tape and pouring a measured solution into the bowl thus created. For the hyperbola, a tub surrounds the lower half of the mirror and forms a bowl into which the measured solution can be poured.

To begin a polishing run, the surface deviation data are read into the computer. For each tool step, the surface deviation data are interpolated to calculate the error at the point of contact between the tool and mirror. Then the tool is moved horizontally using the lead screw until the edge of the tool just touches the end of the blank. At this point the computer sends a series of commands to a pulse generator which drives a stepper motor to advance the lead screw until the center of the tool is over the starting point on the mirror. Rotation of the element and tool is started, and the computer begins sending commands to step

a. Shape assumed while polishing parabola.

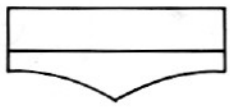

b. Shape assumed while polishing hyperbola.

Figure 21. Tool assumes a conical profile during polishing: (a) Shape assumed while polishing parabola. (b) Shape assumed while polishing hyperbola.

the tool to successive axial positions along the element, allowing it to dwell long enough to remove the error at that axial position. The tool is allowed to remain a certain minimum time even at low positions so that the element will be polished out over the entire aperture. When the polishing run is finished, the element is measured to determine the new profile and whether more polishing is needed.

Certain precautions must be taken when going through the measurement and polishing cycle. One such precaution is to take into account the change in the contact point of the tool relative to the tool center as the tool steps across the mirror. This difference, which for this example is as much as 3 mm, is caused by the changing slope of the mirror at different axial positions. Initial tests are performed to determine where the tool contact point is relative to the tool center as the tool advances over the element, and this information is included in the routine which interpolates the surface deviation at the tool contact points. This is further refined by comparing plots of the data before and after a polishing run to determine exactly where polishing has taken place.

The tool dwell time is calculated using the assumption that the tool contact can be approximated as a point. Although not strictly true, this assumption works acceptably well in practice. This assumption leads to the conclusion that the dwell time of the tool at each axial position depends on the height of the error only at one point.

A second assumption of the polishing is that the polishing rate is linear with polishing pressure. The spring which presses the tool against the mirror will experience large deflections as the tool moves across the mirror, as shown in Fig. 22(a). This will cause a change in the spring force, which will in turn cause a change in polishing rate. To alleviate this, the motor is tilted so that the optical axis of the element makes an angle to the horizontal equal to its average grazing angle. The mirror still rotates about its optical axis, as shown in Fig. 22(b), but the axis is no longer horizontal. The residual deflection, caused by the mirror departure from a cone, which the spring experiences is not great enough to cause a noticeable change in the polishing rate.

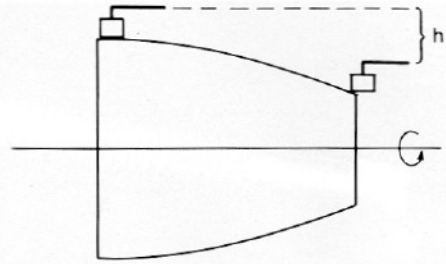

a. With optical axis horizontal.

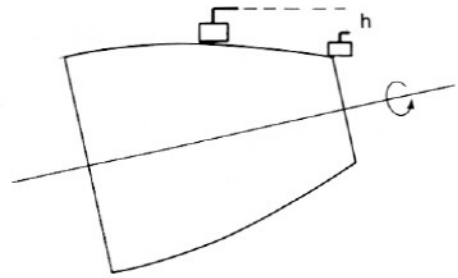

b. With optical axis tilted by amount equal to average slope on mirror.

Figure 22. Change in height experienced by tool as it traverses the mirror: (a) With optical axis horizontal. (b) With optical axis tilted by amount equal to average slope on mirror.

VI. Results

The procedure described above has been applied to elements of the SEUTS telescope. The current figure error of the parabolic primary is shown in Fig. 23(a), and that of the hyperbolic secondary is shown in Fig. 23(b). The parabola has an 0.041-μm (1.6-μin.) rms figure error after 120 h of polishing, and the hyperbola has a rms figure error of 0.054 μm (2.1 μin.) after 30 h of polishing. Figure 24 shows the out-of-roundness of the mirrors after polishing. There is not much difference in the out-of-roundness values before and after polishing, so the polishing process does not seem to introduce out-of-roundness errors. The spatial frequency distribution of the surface errors of the parabola is shown in Fig. 25. The errors with largest amplitude fall in the 0–10/in. frequency range. The amplitudes level out to ~0.3 μin. at high frequencies, and this represents the noise level of the system. The cutoff occurs around 10 cycles/in., so all that is known about their amplitudes is that they are smaller than 0.3 μin. No data are available about errors of correlation length between 0 and 50 μm. Figure 26 shows a comparison of the spatial frequency distribution of surface errors before and after polishing the hyperbola. Errors of frequencies of 0–10 and 30–50 cycles/in. are removed efficiently. However, errors of 10–30-cycles/in. frequency are not removed very efficiently. Various methods are being tested to remove these errors.

Figure 27 shows the expected energies that would be measured by an array of 10- × 10-μm pixels in the focal plane when a point source at 30.4 nm is imaged by the

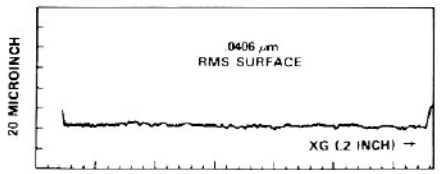

a. Parabola

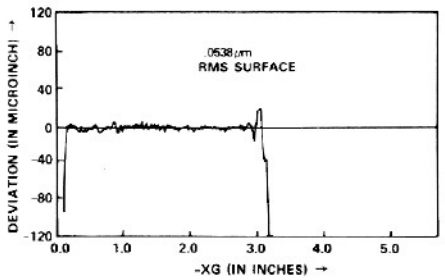

b. Hyperbola

Figure 23. Surface profile of SEUTS mirrors: (a) parabola, (b) hyperbola.

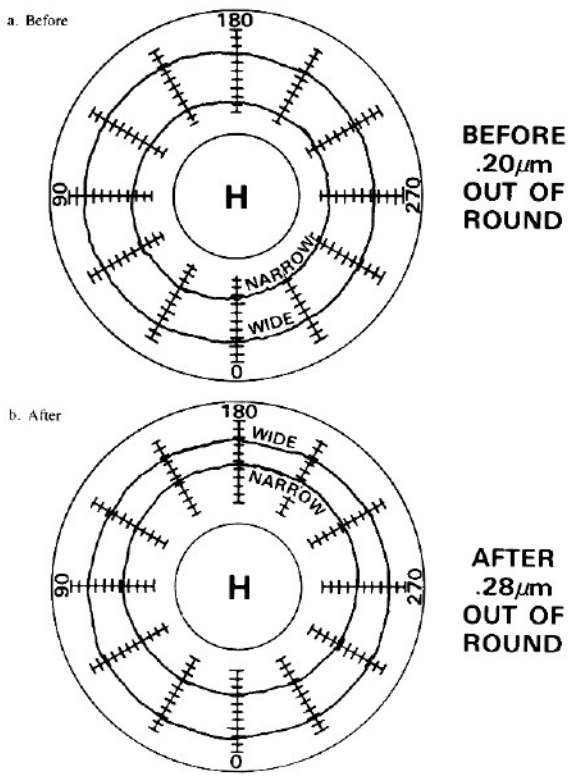

Figure 24. Change in out-of-roundness error introduced by the polishing process in the hyperbola: (a) before, (b) after.

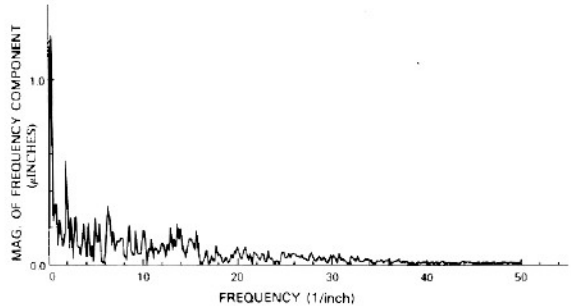

a. Entire aperture, data points taken every .01 inch.

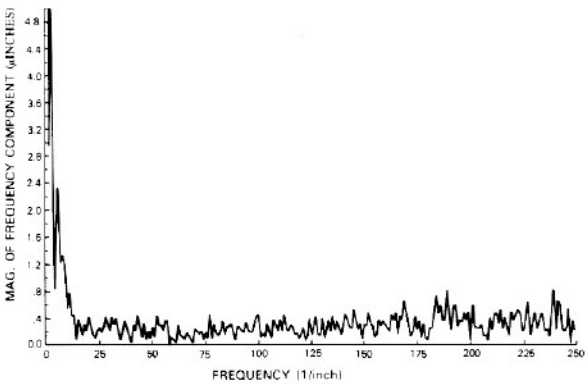

b. One inch segment of aperture. Points taken every .002 inch.

Figure 25. Fourier transform of parabola surface error data: (a) Entire aperture, data points taken every 0.01 in. (b) One inch segment of aperture. Points taken every 0.002 in.

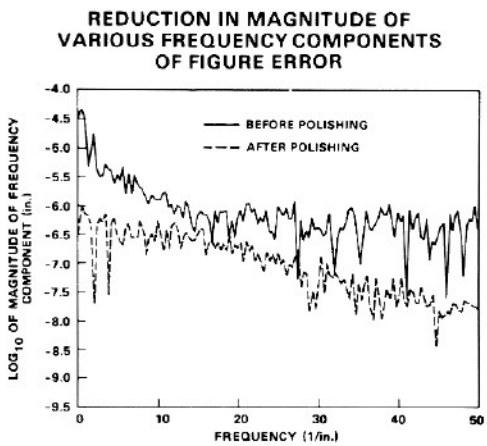

Figure 26. Comparison of spatial frequency distribution of surface errors of hyperbola before and after polishing.

telescope. This was calculated by the optical surface analysis code[18] program, which was developed to evaluate the imaging qualities of manufactured telescopes. The pixel size was chosen to correspond to the width of the focal plane slit in the SEUTS instrument. The full width at half-maximum of the image profile is 45 μm (2.25 sec of arc). There is a significant amount of large angle scatter in the image. The half energy width is 1000 μm (50 sec of arc).

It is the hyperbola which currently limits the performance of the system, as can be seen by looking at Fig. 28, which shows the separate contributions to the image degradation. The hyperbola has not at this point been finished, and its final figure is expected to be as good as that of the parabola. The energies measured by an array of 10- × 10-μm pixels when the hyperbola has the same surface quality as the parabola is shown in Fig. 29. This imaging profile has a full width at half-

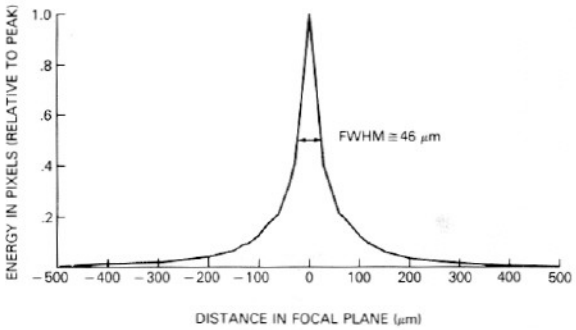

Figure 27. Energies contained in 10- × 10-μm pixels in focal plane of current SEUTS telescope.

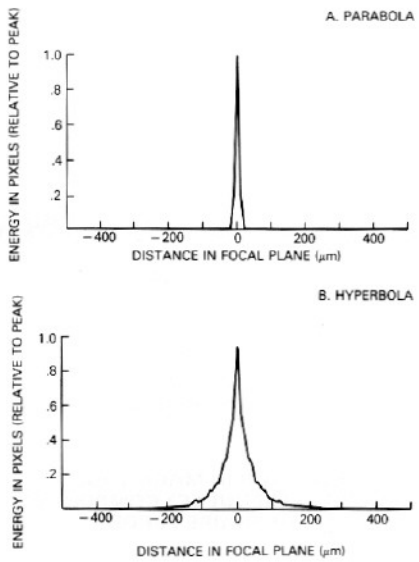

Figure 28. Energies contained in 10- × 10-μm pixels in focal plane when surface errors of the mirrors are considered separately: (a) parabola, (b) hyperbola.

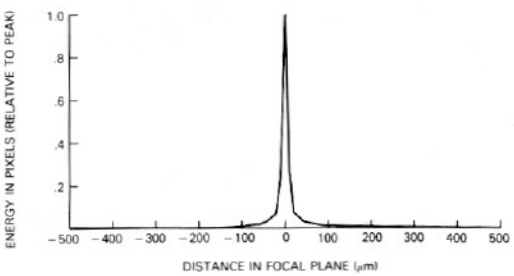

Figure 29. Energies contained in 10- × 10-μm pixels in the focal plane when both mirrors have surface errors the same as the current parabola.

maximum of 15 μm (0.75 sec of arc) and a half energy width of 390 μm (19.5 sec of arc).

VII. Conclusion

We have developed a technique for automating the polishing and testing of the elements of a Wolter type II telescope. The technique allows for fabrication of glancing incidence mirrors with an rms surface error of 0.04 μm or less, which will give images with full width at half-maximum of 0.75 sec of arc and half-energy widths of 19.5 sec of arc when used at a 30.4-nm wavelength.

References

1. W. M. Neupert *et al.*, "A Solar Extreme Ultraviolet Telescope and Spectrograph for Shuttle/Spacelab," Space Sci. Rev. **29,** 425 (1981).
2. W. M. Neupert, "A Solar Extreme Ultraviolet Telescope and Spectrograph for Space Shuttle," NASA Tech. Memo. 80643 (Nov. 1978).
3. W. R. Hunter, D. W. Angel, and G. Hass, "Optical Properties of Evaporated Platinum Films in the Vacuum Ultraviolet from 2200 Å to 150 Å," J. Opt. Soc. Am. **69,** 1695 (1979).
4. L. R. Canfield, G. Hass, and W. R. Hunter, "The Optical Properties of Evaporated Gold in the Vacuum Ultraviolet from 300 Å to 2000 Å," J. Phys. Paris **25,** 124 (1964).
5. R. A. M. Keski-Kuha, "Layered Synthetic Microstructure Technology Considerations for Extreme Ultraviolet," Appl. Opt. **23,** 3534 (1984).
6. J. H. Underwood and T. W. Barbee, "Layered Synthetic Microstructures as Bragg Diffractors for X Rays and Extreme Ultraviolet: Theory and Predicted Performance," Appl. Opt. **20,** 3027 (1981).
7. E. Spiller, A. Segmuller, J. Rife, and R-P. Haelbich, "Controlled Fabrication of Multilayer Soft-X-Ray Mirrors," Appl. Phys. Lett. **37,** 1048 (1980).
8. R-P. Haelbich, A. Segmuller, and E. Spiller, "Smooth Multilayer Films Suitable for X-Ray Mirrors," Appl. Phys. Lett. **34,** 184 (1979).
9. E. Spiller, "Reflective Multilayer Coatings for the Far-UV Region," Appl. Opt. **15,** 2333 (1976).
10. H. Wolter, "Mirror Systems with Glancing Incidence as Imaging-Producing Optics for X-Rays," Ann. Phys. Ser. 6, **10,** 94 (1952).
11. R. A. Jones and N. Geril, "Automated Cylindrical Polishing of Grazing Incidence X-Ray Mirrors," Opt. Eng. 1051 (Nov./Dec. 1982).
12. C. M. Fleetwood and J. D. Mangus, "Fabrication of an Extreme Ultraviolet Glancing Incidence Telescope," Opt. Eng. 159 (Mar/Apr. 1974).
13. A. F. Slomba, "Manufacturing Optimization Study of Lightweighted Cer-vit c-101 Mirrors for Large Space Telescope Applications," Perkin-Elmer Report, NASA contract NAS 5-23293 (3 Nov. 1975).
14. R. Stoll, P. F. Forman, and J. Edelman, "The Effect of Different Grinding Procedures on the Strength of Scratched and Unscratched Fused Silica," in *Symp. Sur La Resistance Micanique du Verre et Ley Moyens de l'Ameliorer*, TA 450 s98 (1961), pp. 377–392.
15. C. M. Fleetwood, R. J. Thomas, and G. A. Wright, "Establishing Fiducials on Glancing Incidence Mirrors," Appl. Opt. **24,** 551 (1985).
16. R. W. Daniels, *An Introduction to Numerical Methods and Optimization Techniques* (Elsevier North-Holland, New York, 1978), pp. 177–264.
17. R. W. Dietz and J. M. Bennett, "Bowl Feed Technique for Producing Supersmooth Optical Surfaces," Appl. Opt. **5,** 881 (1966).
18. P. Glenn and R. Noll, "Optical Surface Analysis Code Final Report," Perkin-Elmer Engineering Report, NASA contract NAS 5-25802 (Mar. 1982).